

Formation of cellular/lamellar nanostructure in Sm₂Co₁₇-type binary and ternary Sm-Co-Zr magnets

Nikita Polin¹, Konstantin P. Skokov², Alex Aubert², Hongguo Zhang^{2,3}, Burçak Ekitli², Esmaeil Adabifiroozjaei⁴, Leopoldo Molina-Luna⁴, Oliver Gutfleisch², Baptiste Gault^{1,5}

¹ Max-Planck Institute for Sustainable Materials, 0237, Düsseldorf 40237, Germany

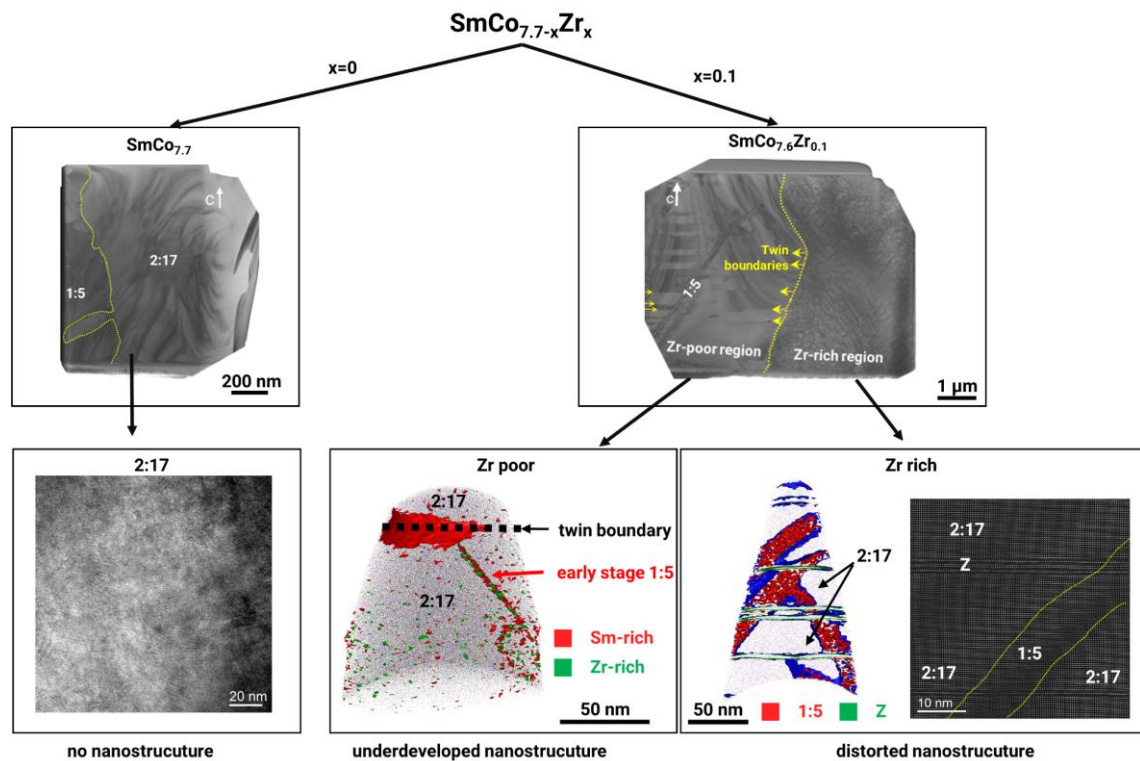
² Functional Materials, Institute of Materials Science, Technical University of Darmstadt, Peter-Grünberg-Str. 16, 64287 Darmstadt, Germany

³ College of Materials Science and Engineering, Key Laboratory of Advanced Functional Materials, Ministry of Education, Beijing University of Technology, Beijing 100124, China

⁴ Advanced Electron Microscopy Division, Institute of Materials Science, Department of Materials and Geosciences, Technische Universität Darmstadt, Peter-Grünbergstrasse 2, Darmstadt 64287, Germany

⁵ Department of Materials, Royal School of Mines, Imperial College, Prince Consort Road, London SW7 2BP, United Kingdom.

Graphical abstract



Highlights

- Zr concentration above 1 at.% promotes cellular/lamellar nanostructure formation in ternary $\text{SmCo}_{7.6}\text{Zr}_{0.1}$
- In absence of Cu, small concentration gradients in the cellular nanostructure cause near zero coercivity in $\text{SmCo}_{7.6}\text{Zr}_{0.1}$
- 2:17 phase twins are suggested to facilitate the formation of 1:5 cell boundary phase

Abstract

2:17 SmCo magnets with a quinary composition of $\text{Sm}(\text{Co,Cu,Fe,Zr})_{7+\delta}$ are industrially-relevant hard magnets used in high temperature and corrosive environments. Their complex cellular/lamellar nanostructure, consisting of ordered 2:17 phase cells, 1:5 phase cell boundaries and Z-phase (Zr-rich) lamellae, is essential for their high coercivity. However, the system's complexity makes it challenging to determine the contribution of each element or microstructural feature to coercivity. To disentangle the microstructure-property relationships, we simplified the system to binary and ternary $\text{SmCo}_{7.7-x}\text{Zr}_x$ (with $x = 0$ and 0.1) magnets and conducted detailed micro- to atomic-scale analyses. Only Zr-containing magnets formed a cellular/lamellar nanostructure akin to industrial magnets, in Zr-rich regions with at least 1 at.% Zr, but without achieving high coercivity due to low elemental gradients in absence of Cu across cell boundaries. Data from Zr-poor areas of $\text{SmCo}_{7.6}\text{Zr}_{0.1}$ suggests that 2:17 phase twin boundaries facilitate cellular nanostructure formation by providing inhomogeneities for heterogeneous nucleation.

Keywords: rare earth magnets, coercivity, atom probe tomography, transmission electron microscopy, cellular/lamellar nanostructure formation

Manuscript

The exceptional magnetic properties of 2:17-type Sm-Zr-Co-Cu-Fe hard magnets at elevated temperatures and in corrosive environments make them ideal for applications like sensors, electric vehicles, renewable energy and aeronautics [1–4].

Industrially sintered magnets have a quinary composition of $\text{Sm}(\text{CoFeCuZr})_{7\pm 6}$ and consist of $\sim 100 \mu\text{m}$ diameter grains, textured along the c-axis of the $\text{Sm}_2\text{Co}_{17}$ phase. These grains exhibit a cellular/lamellar nanostructure with three main components [5,6]: the matrix $\text{Sm}_2(\text{CoFeCuZr})_{17}$ (2:17) phase forms cells ($\sim 100 \text{ nm}$), separated by the $\text{Sm}(\text{CoCuFeZr})_5$ (1:5) phase cell boundaries ($\sim 10 \text{ nm}$) and intersected by the Zr-rich (Z) phase lamellae ($< 10 \text{ nm}$) with stoichiometry close to $\text{Sm}(\text{CoZrFeZr})_3$ perpendicular to the c-axis of $\text{Sm}_2\text{Co}_{17}$. This nanostructure forms during heat treatment, called precipitation hardening or aging, and is crucial for high coercivity [7,8].

The genesis of this cellular/lamellar nanostructure [9–12], as well as other factors influencing the magnets' coercivity, have been extensively studied for the quinary Sm-Zr-Co-Cu-Fe system, including composition [1,12–17], heat treatment parameters [6,12,18–22], stacking faults [23], oxidation [24], grain boundary hydrogen charging [25] and addition of non-magnetic particles [26,27]. However, the inherent complexity of this multicomponent, multiphase system makes isolating the role of each microstructural parameter on coercivity rather challenging. By reducing the alloy complexity, we can investigate step by step the formation of nanostructure and the development of coercivity. Here, we reduced the number of elements and defects by focusing on single grains (eliminating grain boundaries effects) of binary $\text{SmCo}_{7.7}$ and ternary $\text{SmCo}_{7.6}\text{Zr}_{0.1}$.

Few studies from the 2000s on precipitation hardened 2:17 type ternary Sm-Co-Zr alloys [2,15,16,28], found near-zero coercivity despite the presence of cellular/lamellar nanostructure, attributed to the lack of a large domain wall energy gradient across the 1:5 boundaries in absence of Cu [2,16]. However, the reported data lacked detailed structural and compositional data of the nanostructure needed to fully understand this absence of coercivity.

Here, using advanced microstructural characterization techniques including transmission electron microscopy (TEM) and atom probe tomography (APT), we provide the missing data on crystal structures, sizes and microchemistry of the nanostructure. We identified a 1 at.% Zr threshold for nanostructure formation and found further evidence for 2:17 twins enabling cellular structure formation [29]. Our findings enhance understanding of the cellular/lamellar nanostructure's genesis and enable a more rational design of quinary 2:17 Sm-Zr-Co-Cu-Fe alloys.

Elemental Sm, Co, and Zr (>99% purity) were alloyed via induction melting. The nominal compositions, $\text{SmCo}_{7.7}$ and $\text{SmCo}_{7.6}\text{Zr}_{0.1}$, are used throughout this study. To compensate for Sm loss during melting and annealing, 5 wt.% Sm was added. The molten alloys were crushed, wrapped in Mo-foil, sealed in a quartz tube under Ar, annealed at 1180°C for 1 hr for homogenization, and quenched in water. The alloys were aged at 850°C for 18 hrs, cooled to 400 °C at 0.5 K/min, held for 4 hrs, following protocols for quinary Sm-Zr-Co-Cu-Fe alloys [4], and subsequently crushed into single grains with sizes around 0.5 mm.

Magnetic properties were measured on single grains of $\text{SmCo}_{7.7-x}\text{Zr}_x$ with the easy axis aligned along the external magnetic field direction using a room temperature vibrating sample magnetometer (VSM), without demagnetization field correction.

For microstructure analysis, the single grains were aligned in a magnetic field with the *c*-axis out of plane, confirmed by electron-backscattered diffraction (EBSD), then embedded in a solid polymer, grinded, and polished. Microstructure was conducted by scanning electron microscopy (SEM, FEI Helios Nanolab 600i) using the backscatter electron mode (BSE), energy dispersive spectroscopy (EDX, FEI Helios Nanolab 600i) and electron backscatter diffraction (EBSD, Zeiss SIGMA 500). Magnetic domain imaging was performed by magneto-optical Kerr effect (MOKE evico magnetics GmbH) polarized light microscopy (Zeiss Axio Imager.D2m).

Electron transparent specimens for transmission electron microscopy (TEM) were cut out by Ga focused ion beam (FIB) in a SEM/FIB system (Dual-Beam Helios Nanolab 600i, FEI). Bright-field (BF) TEM imaging and selected-area electron diffraction (SAED) measurements were conducted in a conventional transmission electron microscope (JEOL JEM 2100F). High-resolution high angle annular dark field (HAADF) scanning TEM (STEM) imaging was carried out in an aberration-corrected system (JEOL JEM-ARM200F) operated at 200 kV.

For nanoscale composition, needle-shaped specimens were prepared by a Ga focused ion beam (FIB) (Dual-Beam Helios Nanolab 600i, FEI), following the procedure by Thompson et al. [30], using a low energy (5 keV) Ga beam for final milling to remove beam-damaged regions. These specimens were analysed using a CAMECA LEAP 5000 XS atom probe, operating at 40 K under ultra-high vacuum (10^{-10} mbar), with pulsed UV laser (355 nm wavelength, 10 ps pulse duration, 40 pJ pulse energy, 200 kHz pulse rate) and a 1-2% detection rate. Datasets with at least 50 million ions were analyzed AP Suite v.6.3 by CAMECA.

Figure 1 shows the magnetic hysteresis curves of $\text{SmCo}_{7.7}$ and $\text{SmCo}_{7.6}\text{Zr}_{0.1}$ single grains. Saturation occurs at ~ 0.5 T for $\text{SmCo}_{7.7}$ and ~ 1 T for $\text{SmCo}_{7.6}\text{Zr}_{0.1}$. Both samples exhibit near-zero coercivity, with $\text{SmCo}_{7.6}\text{Zr}_{0.1}$ showing slightly higher coercivity than $\text{SmCo}_{7.7}$, at $\mu_0 H_C \sim 20$ mT and ~ 10 mT, respectively.

SEM-BSE mode images in **Figure 2a** reveal microstructural difference between the samples. $\text{SmCo}_{7.7}$ (**Figure 2a1**) displays a dark-contrast matrix phase and bright phase elongated inclusions, ~ 50 μm thick with an irregular shape. Matrix and inclusions are identified as $\text{Sm}_2\text{Co}_{17}$ (2:17) and SmCo_5 (1:5), respectively, as confirmed by EDX (**Table 1**). Smaller 2:17 islands are found within the 1:5 phase.

$\text{SmCo}_{7.6}\text{Zr}_{0.1}$ (**Figure 2a2**) exhibits dark contrast elongated inclusions (20 - 200 μm long, 10 - 20 μm wide), set in a brighter matrix. These inclusions are slightly richer in Sm (~ 1 at.%) and Zr (~ 0.5 at.%) and poorer in Co (~ 1.5 at.%), based on EDX (**Table 1**). EBSD (**Figure S 1f**) confirms a uniform [0001] orientation of matrix and inclusions with grain size > 500 μm . The intermediate grey contrast zones between inclusions and matrix (**Figure 2a2** bottom) result from their superposition as shown by TEM below. The phase assignment is ambiguous in the Sm-Co-Zr diagram [31], so matrix and inclusions are referred to as Zr-rich and Zr-poor regions.

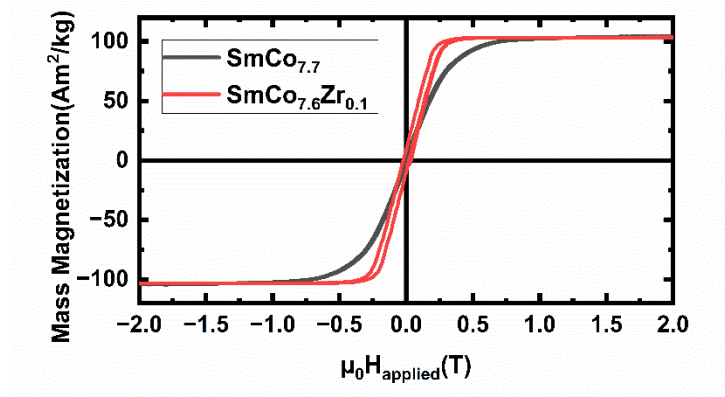


Figure 1 Magnetic hysteresis curves of $\text{SmCo}_{7.7}$ and $\text{SmCo}_{7.6}\text{Zr}_{0.1}$, measured along the magnetically easy c -axis.

Figure 2b illustrates surface magnetic domain structures in Kerr microscopy images of the single grains, with nominal c -axis out of plane. In $\text{SmCo}_{7.7}$ (**Figure 2b1**), inclusions with coarser star-like domains resemble 1:5 phase, while finer domain regions match 2:17 phase. These structures are typical of high anisotropy magnets [32–34], indicating the single crystalline nature of both phases. The domain width of the 1:5 phase is larger compared to the 2:17 phase due to the higher anisotropy constant K_1 of the former [33,35], as the other two intrinsic magnetic properties, spontaneous magnetization J_s and exchange stiffness constant A , have rather similar values.

In $\text{SmCo}_{7.6}\text{Zr}_{0.1}$ (**Figure 2b2**) finer domain inclusions correspond to Zr-poor regions, while coarser domain areas match the Zr-rich regions. The magnetic microstructure of the Zr-poor region resembles the 2:17 matrix phase in $\text{SmCo}_{7.7}$ (**Figure 2b1**), while for Zr-rich regions it resembles non-optimally cooled quinary $\text{Sm}(\text{CoFeCuZr})_{7.2}$ alloys with near zero coercivity [17]. This suggests the presence of 2:17 phase in Zr-poor regions and of cellular nanostructure in the Zr-rich regions.

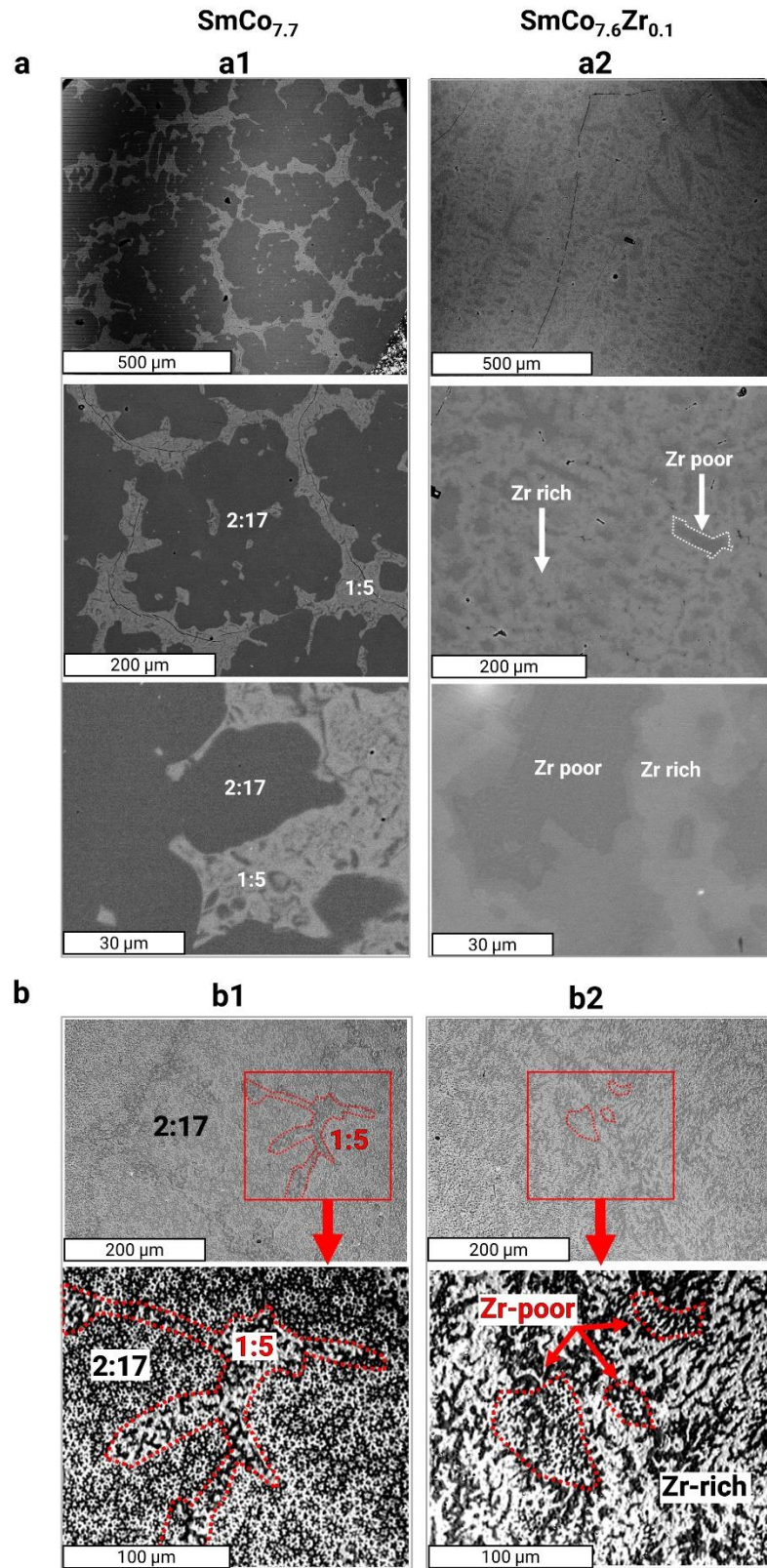


Figure 2 **a** Scanning Electron Microscopy in Backscatter Electron Mode (BSE SEM) and **b** magnetic domain structure by Kerr microscopy for SmCo_{7.7} (left column, **a1**, **b1**) and SmCo_{7.6}Zr_{0.1} (right column **a2**, **b2**). For Kerr and BSE, magnification increases from top to bottom. For all images the nominal *c*-axes of the single grains are oriented out of plane.

Table 1 Compositions in respective regions of $\text{SmCo}_{7.7}$ and $\text{SmCo}_{7.6}\text{Zr}_{0.1}$ as determined by EDX and APT. For the composition column, Sm subscript was set to 1 for easier comparison

Sample	Method	Region	Sm (at. %)	Co (at. %)	Zr (at. %)	Composition
$\text{SmCo}_{7.7}$	EDX	2:17 phase	11.77	88.23	-	$\text{SmCo}_{7.50}$
		1:5 phase	16.8	83.2	-	$\text{SmCo}_{4.95}$
$\text{SmCo}_{7.6}\text{Zr}_{0.1}$	EDX	Zr poor	12.21	86.91	0.87	$\text{SmCo}_{7.12}\text{Zr}_{0.07}$
		Zr-rich	13.41	84.85	1.73	$\text{SmCo}_{6.33}\text{Zr}_{0.13}$
	APT	Zr poor	10.99	88.26	0.75	$\text{SmCo}_{8.03}\text{Zr}_{0.07}$
		Zr-rich	12.75	85.82	1.43	$\text{SmCo}_{6.73}\text{Zr}_{0.11}$

In **Figure 3a1**, BF TEM images of $\text{SmCo}_{7.7}$ confirm phase separation into 1:5 and 2:17R phases, validated by electron diffraction (**Figure S2**). No cellular or lamellar nanostructure is evident in either the electron diffraction images or the HRTEM image of the 2:17 phase (**Figure 3a2**).

In $\text{SmCo}_{7.6}\text{Zr}_{0.1}$, the BF image (**Figure 3b1**) reveals distinct Zr-poor and Zr-rich regions, separated by a well-defined boundary without an intermediate zone. The Zr-poor region primarily consists of the 2:17R phase, enriched in 2:17 twins, as seen from abrupt contrast variations in the BF image and supported by electron diffraction (**Figure S2**), with an estimated area boundary density of $2.7 \mu\text{m}^{-2}$ [36]. A single 100 nm thick 1:5 phase stripe is inclined at 35° to the c-axis. No cellular nanostructure was observed, aligning with Kerr microscopy results.

The Zr-rich region in $\text{SmCo}_{7.6}\text{Zr}_{0.1}$ exhibits a developed cellular and lamellar nanostructure, evident from BF images (**Figure 3b1** and **2b2**), HR-TEM images (**Figure 3c1**) and confirmed by electron diffraction (**Figure S2**). Compared to typical quinary Sm-Co-Cu-Fe-Zr alloys [1,7,11], three key distinctions are noted: First, the 2:17R phase cells are closer to parallelograms, unlike the typical diamond shape, with unequal lengths of 50 – 200 nm. Second, the Z-platelets are relatively thin and,

third, not always continuous, with an average thickness to 1.6 nm based on FFT (reflection at $\frac{1}{4}$ (003)), smaller than the 5-10 nm typical in quinary alloys. Atomic resolution HAADF images (**Figure 3d1 and 2d2**), confirm the atomic structures of the phases, classifying the observed Z-phase as type II [37]. Additionally, a single 2:17 layer between two Z-platelets resembles the observations 1:5 phase layers between Z-platelets in quinary Sm-Co-Cu-Fe-Zr magnets [38].

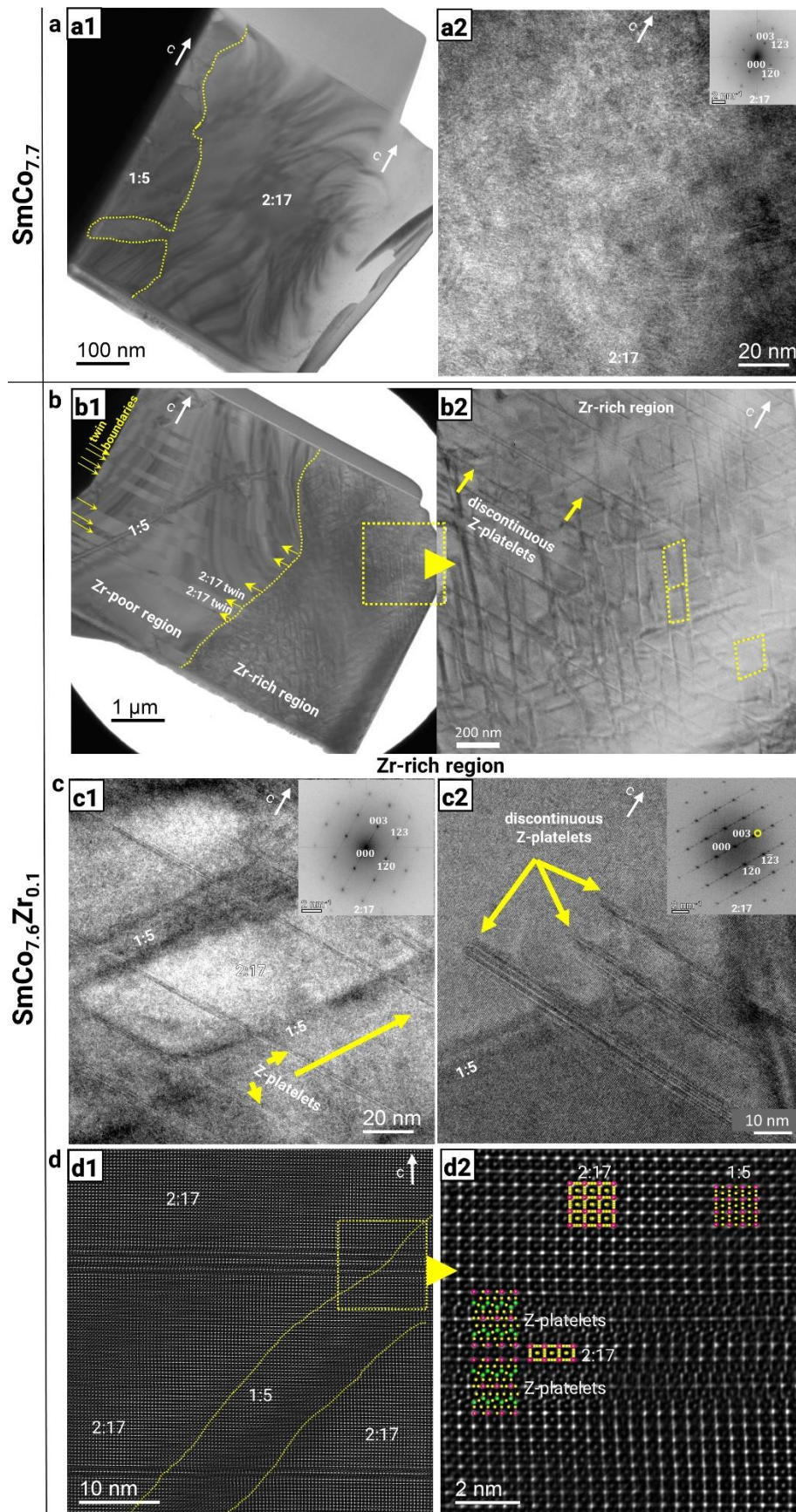


Figure 3 TEM and STEM Characterization of $\text{SmCo}_{7.7}$ (**a**) and $\text{SmCo}_{7.6}\text{Zr}_{0.1}$ (**b-d**) with insets being FFTs of the respective image. **a** TEM images of $\text{SmCo}_{7.7}$: **a1** low magnification BF image with phase boundary between 1:5 and 2:17R phases in $\text{SmCo}_{7.7}$ marked in dashed yellow and **a2** HR-TEM of the 2:17 phase in $\text{SmCo}_{7.7}$ (b) BF TEM images of $\text{SmCo}_{7.6}\text{Zr}_{0.1}$ at **b1** low magnification illustrating the Zr-poor and Zr-rich regions, with boundary in dashed yellow and **b2** digitally magnified view on the Zr-rich region with parallelogram shaped cells marked dashed yellow. **c** High magnification TEM images of $\text{SmCo}_{7.6}\text{Zr}_{0.1}$ within the Zr-rich region: **c1** HR TEM, **c2** high magnification BF TEM. **d** Filtered HAADF STEM images of $\text{SmCo}_{7.6}\text{Zr}_{0.1}$ at **d1** low and **d2** high magnification with overlaid crystal structures of the corresponding phases.

Figures 4a1 and **b1** present 3D APT reconstructions for $\text{SmCo}_{7.6}\text{Zr}_{0.1}$, showing Zr-rich and Zr-poor regions. The *c*-axis aligns with the APT specimen's main axis, confirmed by the Z-platelets' orientation and atom probe crystallographic analysis [39] (**Figure S4**). APT reveals that Zr-rich regions contain more Sm (~2 at.%) and Zr (~0.7 at.%) and less Co (~2.5 at.%) compared to Zr-poor regions, consistent with EDX data (**Table 1**). Using isoconcentration surfaces, the data are segmented into Sm-rich (red) and Zr-rich (green) areas with thresholds reported in caption of **Figure 4**.

In the Zr-rich region of $\text{SmCo}_{7.6}\text{Zr}_{0.1}$ (**Figure 4a**), Sm-rich and Zr-rich areas correspond to 1:5 phase and Z-phase, the former having the highest solubility of Sm and the latter for Zr compared to competing phases [40,41]. The interfaces to the 2:17 phase are marked in blue. A 3D network of ~10 nm thick 1:5 phase cell boundaries surrounds parallelogram-shaped 2:17 cells, with ~5 nm thick Z-platelets intersecting perpendicular to the *c*-axis, as seen from the complete APT dataset (**Figure 4a1**) and a 10 nm-thick dataset slice (**Figure 4a2**). Although the cell size could not be estimated due to the limited field-of-view of APT, the observed nanostructure agrees with TEM.

Phase composition from representative 1D profiles (**Figures 4a3 and 3a4**) are: $\text{Sm}_1\text{Co}_{5.1}\text{Zr}_{0.1}$ for the 1:5-phase (arrow #1), $\text{Sm}_1\text{Co}_{10.9}\text{Zr}_{1.9}$ for the Z-phase (arrow #2) and $\text{Sm}_2\text{Co}_{16.1}\text{Zr}_{0.1}$ for the 2:17 phase. The 1:5 phase has ~ 0.5 at.% more Zr than 2:17 phase, indicating higher Zr solubility, likely due to preference of Zr to occupy the Sm-sublattice due to similar atomic radius [31]. Zr concentration and stoichiometry (Sm+Zr to Co) in the Z-phase, close to 1:4, resemble quinary Sm-Co-Fe-Cu-Zr magnets [38,42,43]. The elemental gradients across the 1:5-2:17 phase boundary (in $\text{at. \%} \cdot \text{nm}^{-1}$ for Sm; Co; Zr : 2.3; 2.4; 0.3) are much smaller than in quinary Sm-Co-Fe-Cu-Zr magnets ($6 - 18 \text{ at. \%} \cdot \text{nm}^{-1}$ for Cu) [38,43].

In the Zr-poor region of $\text{SmCo}_{7.6}\text{Zr}_{0.1}$, the 3D composition map and 3D point cloud (**Figure 4b1 and b2**) reveal a mostly homogeneous elemental distribution, with composition $\text{Sm}_2\text{Co}_{16.06}\text{Zr}_{0.14}$ close to 2:17 stoichiometry with Sm-excess and 0.1 at.% dissolved Zr. However, distinct features were identified, with compositions taken from 1D profiles (**Figures 4b3 and b4**): (1) A planar, mostly segregation free feature, identified as a twin boundary based on atom probe crystallography analysis [39] (**Figure S 4, Figure S 3**); (2) A Sm-Zr-rich planar feature adjacent to the twin boundary (arrow #3), inclined at $\sim 40^\circ$ to (006) planes and coherent with the 2-17 phase (**Figure S 3**), with composition $\text{Sm}_1\text{Co}_{6.6}\text{Zr}_{0.1}$ indicating early-stage 1:5 phase with Co excess and a Sm deficit; (3) A Sm-rich feature (arrow #4) partially covering the twin boundary, with a composition $\text{Sm}_1\text{Co}_{1.48}\text{Zr}_{0.02}$ not assignable to any known phase from the phase diagram [44], indicative for a metastable phase, possibly formed due to local fluctuations of Sm, Co and Zr. These features were observed in one out of three APT measurements, with the others showing a homogenous distribution, consistent with twin density in TEM.

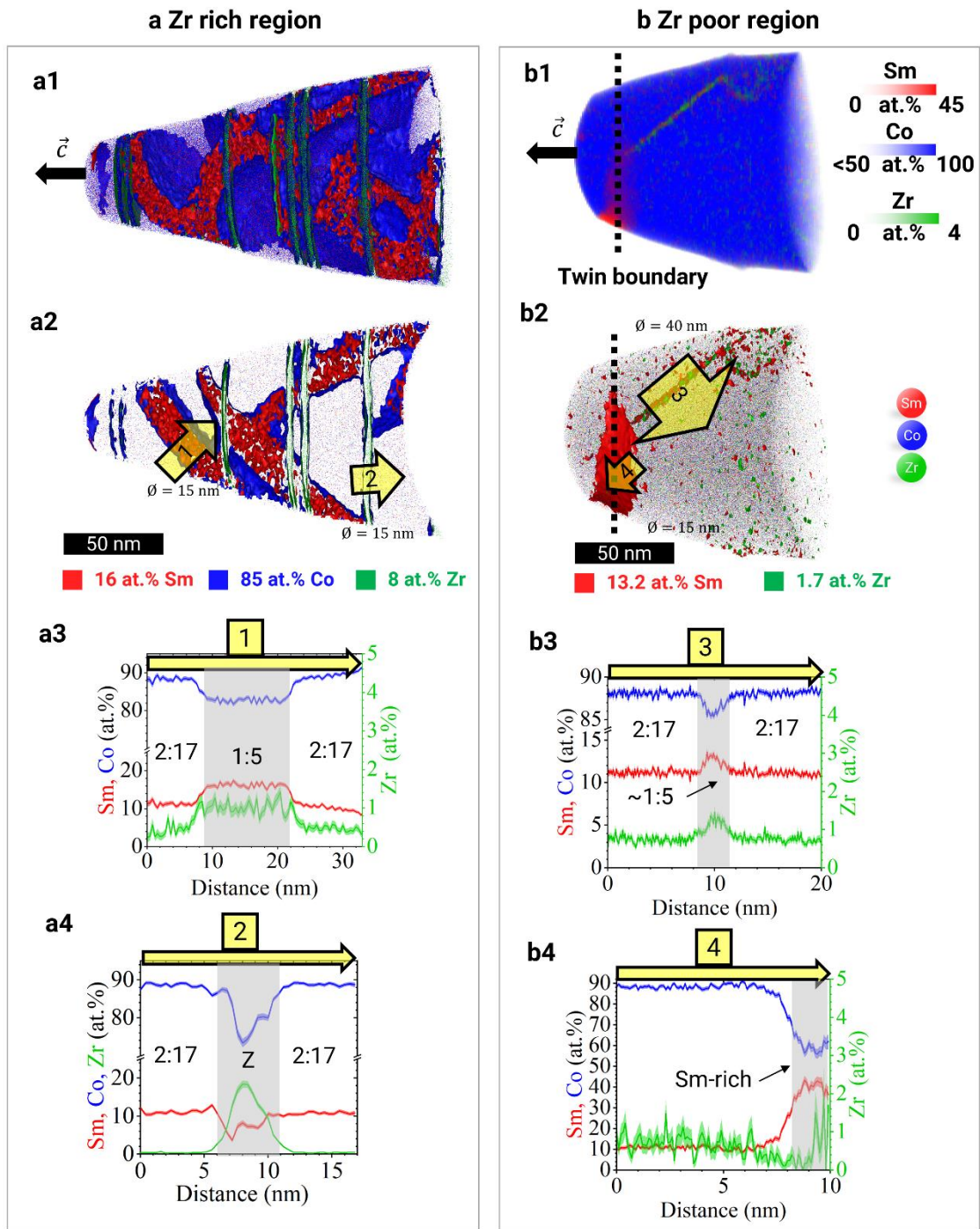


Figure 4 3D APT characterization of $\text{SmCo}_{7.6}\text{Zr}_{0.1}$ in the respective regions – **a** Zr-rich region and **b** Zr-poor region. **a1-a2** Complete dataset and 10-nm slice of the 3D APT reconstructions for Zr-rich region showing the geometrical distribution of the 1:5 phase (red, isoconcentration value 16 at.% Sm), the Z-phases (green, isoconcentration value 8 at.% Zr) and their interfaces to the 2:17 phase (blue, isoconcentration value 85 at.% Co). **b1-b2** 3D concentrations and 3D APT reconstruction for

Zr-poor region revealing an early stage 1:5 phase and Sm-rich feature at the twin boundary using isosurfaces for Sm (red, isoconcentration value 13.2 at.% Sm) and Zr (green, isoconcentration value 1.7 at.% Zr). **a3,a4,b3,b4** representative 1D profiles across features observed in the 3D APT data as indicated by enumerated yellow arrows.

Figure 5 summarizes our findings on the roles of (1) Zr and (2) twins in cellular/lamellar nanostructure formation in $\text{SmCo}_{7.7-x}\text{Zr}_x$, and (3) the impact of chemical gradients on coercivity.

(1) In $\text{SmCo}_{7.7}$ (no Zr), only separated 1:5 and 2:17R SmCo phases form, without any nanostructure, consistent with literature [16,31]. During homogenization at 1180°C, the absence of Zr prevents stabilization of a high-temperature phase, likely causing alloy decomposition before quenching [31]. Zr addition, however, enables the metastable 2:17H phase, ensuring alloy homogeneity before quenching [31].

In $\text{SmCo}_{7.6}\text{Zr}_{0.1}$ (with Zr), regions with over 1 at.% Zr (Zr-rich) form a cellular/lamellar nanostructure with distorted cells and discontinuous, thin Z-platelets, while insufficient Zr < 1at.% leads to undesired Zr-poor regions without a developed cellular/lamellar nanostructure. To our knowledge, the 1 at.% Zr threshold for nanostructure formation in SmCo based alloys has not been previously reported. Optimized Zr content and longer homogenization may eliminate Zr-poor regions and promote an optimal nanostructure throughout the sample.

(2) The Zr-poor regions are rich in 2:17 twins, which were suggested to aid lamellar [1,4,45] and cellular [29] nanostructure formation during the heat treatment process for quinary Sm-Zr-Co-Cu-Fe magnets. Twins are common in magnetic systems [46–48] and may be induced by quenching stresses, similar to carbon steels [49]. Early-stage cellular nanostructure formation, as suggested by Wu et al. [29], is miti-

gated by 2:17R microtwin migration, creating antiphase boundaries, serving as nucleation centers for the 1:5 cell boundary phase as well as for Cu/Fe elemental segregation in this phase. The presence of the 1:5 phase in Zr-poor regions, observed at low fractions and thicknesses of 4-100 nm, indicates such an early-stage cellular nanostructure, similar to Sm-Zr-Co-Cu-Fe magnets at the early-stage of heat treatment [18,19]. This underdeveloped structure likely results from the local Zr deficit, with the 4 nm-thick early-stage 1:5 phase, as revealed by APT, potentially representing an antiphase boundary. This finding further evidences 2:17R twins to aid cellular nanostructure formation.

(3) Both alloys exhibit near-zero coercivity: in SmCo_{7.7} due to absence of a developed nanostructure, in SmCo_{7.6}Zr_{0.1} despite a cellular/lamellar nanostructure present in >50% of the sample's volume. Similar findings were attributed to small concentration gradients across the cellular phase in Sm-Co-Fe-Ni-Zr alloys [12] and non-aged Sm-Zr-Co-Cu-Fe alloys [16,34]. In SmCo_{7.6}Zr_{0.1}, small gradients in Sm, Co and Zr across the 1:5/2:17R phase boundaries, and the absence of gradients within the 1:5 phase itself, results in minimal domain wall energy gradients and near-zero coercivity, as was proposed in previous studies for these alloys [2,16]. APT quantitatively confirmed these small gradients for SmCo_{7.7-x}Zr_x, highlighting that nanostructure alone does not guarantee high coercivity in SmCo magnets.

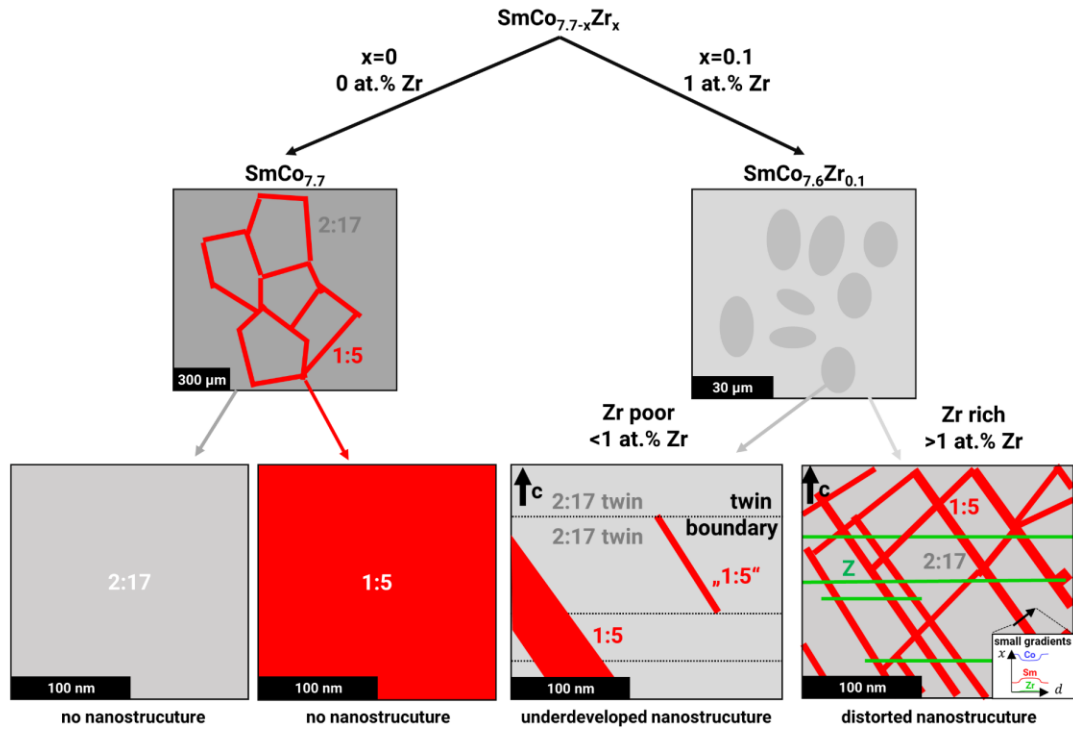


Figure 5 Schematic representation of microstructure (top) and nanostructure (bottom) of $\text{SmCo}_{7.7-x}\text{Zr}_x$ alloys with $x = 0$ and 0.1 : without Zr addition ($\text{SmCo}_{7.7}$, left), the alloy separates into two pure phases being 1:5 and 2:17 phases without any cellular/lamellar nanostructure. With addition of Zr ($\text{SmCo}_{7.6}\text{Zr}_{0.1}$, right) into the alloy, two regions form with slightly different Zr and Sm content form: the Zr-poor region forms a strongly underdeveloped cellular nanostructure consisting of twinned 2:17R phase and rarely found 1:5 phase, while a Zr-rich region forms a distorted cellular/lamellar nanostructure consisting of parallelogram shaped cells of 2:17R phase, 1:5 phase cell boundaries and discontinuous, thin Z-platelets with low gradients across the 1:5/2:17 phase boundary. Around 1 at. % Zr is needed for nanostructure formation.

In conclusion, magnetic properties and microstructure of aged $\text{SmCo}_{7.7}$ and $\text{SmCo}_{7.6}\text{Zr}_{0.1}$ single grains were analyzed from meso to nanoscale. Without Zr, the necessary cellular/lamellar nanostructure fails to develop, leading to mesoscale phase separation. Adding Zr above 1 at.% enables the desired nanostructure, akin to quinary Sm-Zr-Co-Cu-Fe magnets. Insufficient Zr in $\text{SmCo}_{7.6}\text{Zr}_{0.1}$ results in distorted cells and thin, discontinuous lamellae in the Zr/Sm-rich regions and creates

Zr/Sm-poor regions, characterized by 2:17 phase enriched in twins, which likely contribute to nucleation of minor 1:5 phases.

Near-zero coercivity in $\text{SmCo}_{7.7}$ is due to absence of a developed nanostructure, while for $\text{SmCo}_{7.6}\text{Zr}_{0.1}$, it is due to minimal elemental gradients across the cellular nanostructure, resulting in low domain energy gradients. The study emphasizes the significant role of Zr and 2:17 twins in promoting cellular/lamellar nanostructure formation, while also underscoring the importance of nanoscale chemical gradients to attain high coercivity in SmCo magnets.

Acknowledgments

We thank Uwe Tezins, Christian Broß, and Andreas Sturm for their support to the FIB & APT facilities at MPIE. NP is grateful for the financial support from International Max Planck Research School for Sustainable Metallurgy (IMPRS-SusMet). We thank the Collaborative Research Centre/Transregio 270 HoMMage and all project partners for the fruitful discussions and scientific input. This work was supported by the Deutsche Forschungsgemeinschaft (DFG, German Research Foundation), Project ID No. 405553726, TRR 270.

Declaration of Competing Interest

The authors declare that they have no known competing financial interests or personal relationships that could have appeared to influence the work reported in this paper.

Literature

- [1] M. Duerrschnabel, M. Yi, K. Uestuener, M. Liesegang, M. Katter, H.-J. Kleebe, B. Xu, O. Gutfleisch, L. Molina-Luna, Atomic structure and domain wall pinning in samarium-cobalt-based permanent magnets, *Nat. Commun.* 8 (2017) 54.
- [2] G.C. Hadjipanayis, W. Tang, Y. Zhang, S.T. Chui, J.F. Liu, C. Chen, H. Kronmüller, High temperature 2:17 magnets: Relationship of magnetic properties to microstructure and processing, *IEEE Trans. Magn.* 36 (2000) 3382–3387.
- [3] J.F. Liu, Y. Zhang, D. Dimitrov, G.C. Hadjipanayis, Microstructure and high temperature magnetic properties of $\text{Sm}(\text{Co,Cu,Fe,Zr})_z$ ($z=6.7\text{--}9.1$) permanent magnets, *J. Appl. Phys.* 85 (1999) 2800–2804.
- [4] O. Gutfleisch, High-Temperature Samarium Cobalt Permanent Magnets, in: *Nanoscale Magn. Mater. Appl.*, Springer US, Boston, MA, 2009: pp. 337–372.
- [5] F. Okabe, H.S. Park, D. Shindo, Y.-G. Park, K. Ohashi, Y. Tawara, Microstructures and Magnetic Domain Structures Studied by Transmission Electron Microscopy, 47 (2006) 218–223.
- [6] X.Y. Xiong, T. Ohkubo, T. Koyama, K. Ohashi, Y. Tawara, K. Hono, The microstructure of sintered $\text{Sm}(\text{Co}_{0.72}\text{Fe}_{0.20}\text{Cu}_{0.055}\text{Zr}_{0.025})_{7.5}$ permanent magnet studied by atom probe, *Acta Mater.* 52 (2004) 737–748.
- [7] C. Maury, L. Rabenberg, C.H. Allibert, Genesis of the cell microstructure in the $\text{Sm}(\text{Co, Fe, Cu, Zr})$ permanent magnets with 2:17 type, *Phys. Status Solidi* 140 (1993) 57–72.
- [8] M. Katter, J. Weber, W. Assmus, P. Schrey, W. Rodewald, A New Model for the Coercivity Mechanism of $\text{Sm}_z(\text{Co,Fe,Cu,Zr})_l$, *Magnets*, 32 (1996) 4815–4817.
- [9] A.E. Ray, Metallurgical behavior of $\text{Sm}(\text{Co,Fe,Cu,Zr})_z$ alloys, *J. Appl. Phys.* 55 (1984) 2094–2096.

- [10] A.E. Ray, S. Liu, Recent progress in 2:17-type permanent magnets, *J. Mater. Eng. Perform.* 1 (1992) 183–191.
- [11] H. Kronmüller, D. Goll, Micromagnetism of advanced hard magnetic materials, *Int. J. Mater. Res.* 100 (2009) 640–651.
- [12] C. Wang, M.G. Zhu, Overview of composition and technique process study on 2:17-type Sm–Co high-temperature permanent magnet, *Rare Met.* 40 (2021) 790–798.
- [13] N. Yu, W. Gao, M. Pan, H. Yang, Q. Wu, P. Zhang, H. Ge, Influence mechanism of Fe content on the magnetic properties of Sm₂Co₁₇-type sintered magnets: Microstructure and Microchemistry, *J. Alloys Compd.* 818 (2020) 152908.
- [14] L. Pierobon, R.E. Schäublin, A. Kovács, S.S.A. Gerstl, A. Firlus, U. V. Wyss, R.E. Dunin-Borkowski, M. Charilaou, J.F. Löffler, Temperature dependence of magnetization processes in Sm(Co, Fe, Cu, Zr)₂ magnets with different nanoscale microstructures, *J. Appl. Phys.* 129 (2021).
- [15] W. Tang, Y. Zhang, G.C. Hadjipanayis, H. Kronmüller, Influence of Zr and Cu content on the microstructure and coercivity in Sm(Co_{0.9}Fe_{0.1}Cu_xZr_x)_{8.5} magnets, *J. Appl. Phys.* 87 (2000) 5308–5310.
- [16] W. Tang, Y. Zhang, G.C. Hadjipanayis, Microstructure, magnetic properties and magnetic hardening in 2 : 17 Sm–Co magnets, *Int. J. Mater. Res.* 93 (2022) 1002–1008.
- [17] A. Lefèvre, L. Cataldo, M.T. Cohen-Adad, B.F. Mentzen, A representation of the Sm-Co-Zr-Cu-Fe quinary system: A tool for optimisation of 2/17 permanent magnets, *J. Alloys Compd.* 262–263 (1997) 129–133.
- [18] Y. Zhang, W. Tang, G.C. Hadjipanayis, C. Chen, C. Nelson, K. Krishnan, Evolution of microstructure, microchemistry and coercivity in 2 : 17 type Sm-Co

- magnets with heat treatment, IEEE Trans. Magn. 37 (2001) 2525–2527.
- [19] D. Goll, H. Kronmüller, H.H. Stadelmaier, Micromagnetism and the microstructure of high-temperature permanent magnets, J. Appl. Phys. 96 (2004) 6534–6545.
- [20] A. Yan, A. Bollero, O. Gutfleisch, K.-H. Müller, L. Schultz, Melt-spun precipitation hardened Sm(Co, Fe, Cu, Zr) magnets, Mater. Sci. Eng. A 375–377 (2004) 1169–1172.
- [21] A. Yan, O. Gutfleisch, T. Gemming, K.-H. Müller, Microchemistry and magnetization reversal mechanism in melt-spun 2:17-type Sm-Co magnets, Appl. Phys. Lett. 83 (2003) 2208–2210.
- [22] A. Yan, O. Gutfleisch, A. Handstein, T. Gemming, K.-H. Müller, Microstructure, microchemistry, and magnetic properties of melt-spun Sm(Co,Fe,Cu,Zr)_z magnets, J. Appl. Phys. 93 (2003) 7975–7977.
- [23] X. Song, T. Ma, X. Zhou, F. Ye, T. Yuan, J. Wang, M. Yue, F. Liu, X. Ren, Atomic scale understanding of the defects process in concurrent recrystallization and precipitation of Sm-Co-Fe-Cu-Zr alloys, Acta Mater. 202 (2021) 290–301.
- [24] Y. Zhang, H. Tan, X. Cao, A. Bhowmik, V. Gill, A. Lambourne, A.Q. Yan, Y. Huang, Atomic-scale oxidation of a Sm₂Co₁₇-type magnet, Acta Mater. 220 (2021) 117343.
- [25] X. Ye, F. Yan, L. Schäfer, D. Wang, H. Geßwein, W. Wang, M.R. Chellali, L.T. Stephenson, K. Skokov, O. Gutfleisch, D. Raabe, H. Hahn, B. Gault, R. Kruk, Magnetoelectric Tuning of Pinning-Type Permanent Magnets through Atomic-Scale Engineering of Grain Boundaries, Adv. Mater. 33 (2021) 2–8.
- [26] G. Yan, Z. Liu, W. Xia, C. Zhang, G. Wang, R. Chen, D. Lee, J.P. Liu, A. Yan, Grain boundary modification induced magnetization reversal process and giant

- coercivity enhancement in 2:17 type SmCo magnets, *J. Alloys Compd.* 785 (2019) 429–435.
- [27] H. Chen, Y. Wang, Y. Yao, J. Qu, F. Yun, Y. Li, S.P. Ringer, M. Yue, R. Zheng, Attractive-domain-wall-pinning controlled Sm-Co magnets overcome the coercivity-remanence trade-off, *Acta Mater.* 164 (2019) 196–206.
- [28] W. Tang, A.M. Gabay, Y. Zhang, G.C. Hadjipanayis, H. Kronmüller, Temperature dependence of coercivity and magnetization reversal mechanism in Sm(Co_{0.9}Fe_{0.1}Cu_{0.04}Zr_{0.04})_{7.0} magnets, *IEEE Trans. Magn.* 37 (2001) 2515–2517.
- [29] H. Wu, C. Zhang, Z. Liu, G. Wang, H. Lu, G. Chen, Y. Li, R. Chen, A. Yan, Nanoscale short-range ordering induced cellular structure and microchemistry evolution in Sm₂Co₁₇-type magnets, *Acta Mater.* 200 (2020) 883–892.
- [30] K. Thompson, D. Lawrence, D.J. Larson, J.D. Olson, T.F. Kelly, B. Gorman, In situ site-specific specimen preparation for atom probe tomography, *Ultramicroscopy* 107 (2007) 131–139.
- [31] A.G. Dormidontov, N.B. Kolchugina, N.A. Dormidontov, Y. V. Milov, Structure of alloys for (Sm,Zr)(Co,Cu,Fe)Z permanent magnets: First level of heterogeneity, *Materials (Basel)*. 13 (2020).
- [32] K. Bachmann, A. Bischofberger, F. Hofer, Magnetic domain patterns in small single crystal SmCo₅ particles, *J. Mater. Sci.* 6 (1971) 169–170.
- [33] Alex Hubert, Rudolf Schäfer, *Magnetic domains – the analysis of magnetic microstructures*, 1998.
- [34] O. Gutfleisch, K.H. Müller, K. Khlopkov, M. Wolf, A. Yan, R. Schäfer, T. Gemming, L. Schultz, Evolution of magnetic domain structures and coercivity in high-performance SmCo 2:17-type permanent magnets, *Acta Mater.* 54 (2006)

997–1008.

- [35] J.M.D. Coey, S.S. Stuart, Handbook of Magnetism and Magnetic Materials: Volume 1,2, 2021.
- [36] N. Bozzolo, M. Bernacki, Viewpoint on the Formation and Evolution of Annealing Twins During Thermomechanical Processing of FCC Metals and Alloys, *Metall. Mater. Trans. A* 51 (2020) 2665–2684.
- [37] Y. Zhang, P. Wu, Y. Lu, X. Cao, Y. Huang, V. Gill, Z. Li, Unveiling the anomalous atomic stacking and formation mechanism of 1:3R Z-plates in Sm₂Co₁₇-type magnets, *J. Alloys Compd.* 934 (2023).
- [38] S. Giron, N. Polin, E. Adabifiroozjaei, Y. Yang, A. Kovács, T.P. Almeida, D. Ohmer, K. Üstüner, A. Saxena, M. Katter, I.A. Radulov, C. Freysoldt, R.E. Dunin-Borkowski, M. Farle, K. Durst, H. Zhang, L. Alff, K. Ollefs, B.-X. Xu, O. Gutfleisch, L. Molina-Luna, B. Gault, K.P. Skokov, Towards engineering the perfect defect in high-performing permanent magnets, (2023).
- [39] V.J. Araullo-Peters, B. Gault, S.L. Shrestha, L. Yao, M.P. Moody, S.P. Ringer, J.M. Cairney, Atom probe crystallography: Atomic-scale 3-D orientation mapping, *Scr. Mater.* 66 (2012) 907–910.
- [40] R. Glardon, W. Kurz, Cobalt-Samarium-Copper Phase Diagram., *Zeitschrift Fuer Met. Res. Adv. Tech.* 70 (1979) 386–391.
- [41] A.J. Perry, The constitution of copper-hardened samarium-cobalt permanent magnets, *J. Less-Common Met.* 51 (1977) 153–162.
- [42] H. Sepehri-Amin, J. Thielsch, J. Fischbacher, T. Ohkubo, T. Schrefl, O. Gutfleisch, K. Hono, Correlation of microchemistry of cell boundary phase and interface structure to the coercivity of Sm(Co_{0.784}Fe_{0.100}Cu_{0.088}Zr_{0.028})_{7.19} sintered magnets, *Acta Mater.* 126 (2017) 1–10.

- [43] L. Pierobon, A. Kovács, R.E. Schäublin, S.S.A. Gerstl, J. Caron, U. V. Wyss, R.E. Dunin-Borkowski, J.F. Löffler, M. Charilaou, Unconventional magnetization textures and domain-wall pinning in Sm–Co magnets, *Sci. Rep.* 10 (2020) 1–11.
- [44] P. Villars, H. Okamoto, eds., Co-Sm Binary Phase Diagram 0-100 at.% Sm: Datasheet from “PAULING FILE Multinaries Edition – 2022” in SpringerMaterials (https://materials.springer.com/isp/phase-diagram/docs/c_0904734), (2023).
- [45] H. Feng, H. Chen, Z. Guo, R. Yu, W. Li, Twinning structure in Sm(Co,Fe,Cu,Zr)_z permanent magnet, *Intermetallics* 18 (2010) 1067–1071.
- [46] S. Ener, K.P. Skokov, D. Palanisamy, T. Devillers, J. Fischbacher, G.G. Eslava, F. Maccari, L. Schäfer, L.V.B. Diop, I. Radulov, B. Gault, G. Hrkac, N.M. Dempsey, T. Schrefl, D. Raabe, O. Gutfleisch, Twins – A weak link in the magnetic hardening of ThMn₁₂-type permanent magnets, *Acta Mater.* 214 (2021) 116968.
- [47] D. Palanisamy, D. Raabe, B. Gault, On the compositional partitioning during phase transformation in a binary ferromagnetic MnAl alloy, *Acta Mater.* 174 (2019) 227–236.
- [48] D. Palanisamy, A. Kovács, O. Hegde, R.E. Dunin-Borkowski, D. Raabe, T. Hickel, B. Gault, Influence of crystalline defects on magnetic nanodomains in a rare-earth-free magnetocrystalline anisotropic alloy, *Phys. Rev. Mater.* 5 (2021) 064403.
- [49] A. Samuel, K.N. Prabhu, Residual Stress and Distortion during Quench Hardening of Steels: A Review, *J. Mater. Eng. Perform.* 31 (2022) 5161–5188.

Supplementary Material

A. Microstructure and nanostructure characterization

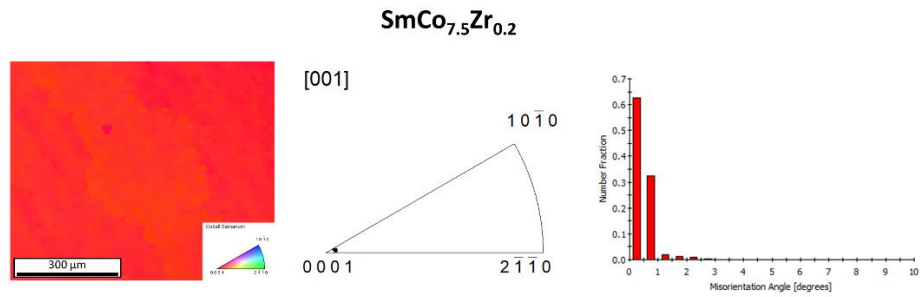


Figure S1 Surface orientation characterization of SmCo_{7.6}Zr_{0.1} by EBSD assuming Sm₂Co₁₇ majorita phase: [001] inverse pole figure map (left), inverse pole figure (middle), misorientation angle distribution (right). The sample has a uniform [001] orientation with misorientaion angles < 1°.

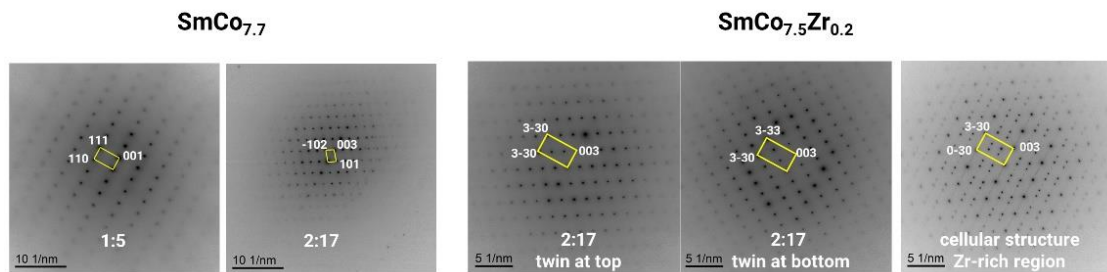


Figure S2 Selected area electron diffraction (SAED) data extracted from regions indicated in **Figure 3**.

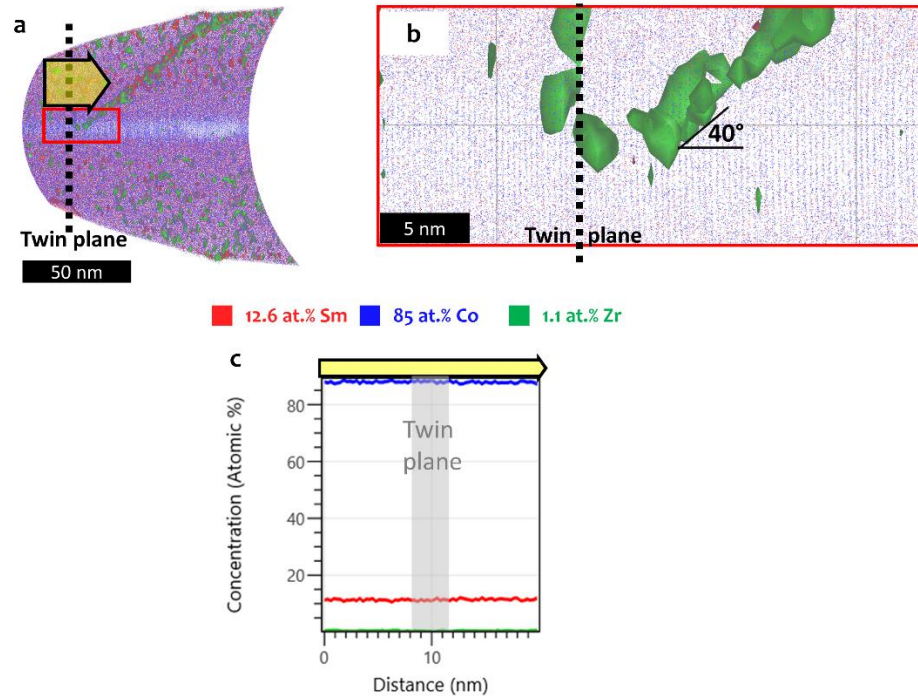


Figure S3 Coherent precipitate close to early-stage 1:5 phase at the twin boundary, in the 3D APT data in the Zr-poor region in the $\text{SmCo}_{7.6}\text{Zr}_{0.1}$ sample. **a** 10 nm slice of the 3D reconstruction of APT data shown in **Figure 4b2**. **b** Atomic planes in z-direction intersect the precipitate close to 1:5 phase in a magnified region of interest as marked by red rectangle in **a**. **c** 1D profile (cylinder 20 nm length and diameter) across the twin plane (yellow arrow in **a**) which exhibits no elemental segregation away from the 1:5-like phase and the the Sm-rich feature. The c-axis remains preserved at the twin plane as expected.

B. Crystallographic analysis

For the crystallographic analysis, the following steps were followed:

1. Extract atomic hit map showing “poles” for the specific region of the APT dataset (i.e. top or bottom twin)
2. Overlay both hit maps with stereographic projection of the 2-17 phase with c-axis out of plane, such that hit maps and stereographic overlap
3. Identify the poles (h k l) in the hit map and in the corresponding 3D data using the Co isovalues
4. Calibrate the reconstruction of the specific region such, that mean distance corresponds to the distance of the main pole or multiples of it: in this case [0006]
5. Measure the distances of identified poles (h k l) in the 3D data from ROIs close to the poles
6. Compare the measured and expected distances of identified poles (h k l): if the values equal, then step the poles were correctly identified. If not, repeat the procedure starting from step 2.

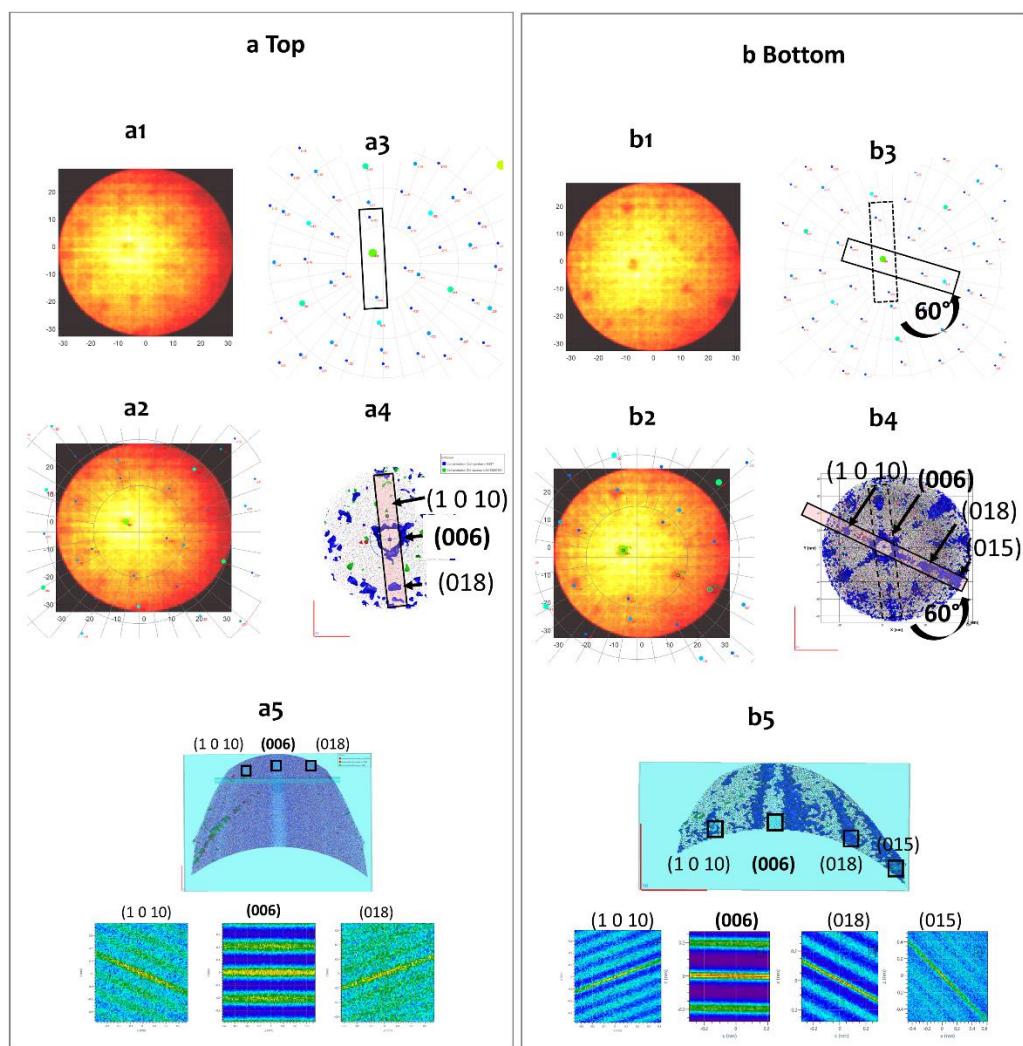


Figure S4 Crystallographic analysis of the of the APT data for **a** Top part and **b** Bottom part for the Zr-poor region $\text{SmCo}_{7.6}\text{Zr}_{0.1}$ dataset: Top and bottom atomic hit maps (a1, b1), stereographic projections (a2,b2), overlay of the former (a3,b3) and slice though the 3D APT data displaying the poles marked by isosurface at 89.7 at% Co (blue), also observed in (a1, b1). (a5,b5) shows spatial density maps in xz-direction (xz-SDMs) extracted from regions of interest close to the poles determined before. Note that the projection of the bottom part is rotated by 60° in respect to the top part as shown by solid and dashed rectangles in b2 and b4 indicating a presence of a twin boundary.

Table S1 Crystallographic analysis of the Zr-poor region SmCo_{7.6}Zr_{0.1} APT data in the Figure S4

Miller indices (hkl) of the poles	expected dis- tances (nm)	measured distances, top region (nm)	measured distances, bottom region (nm)
(006)	0.2	0.2	0.2
(018)	0.15	0.14	0.14
(015)	0.23	-	0.23
(1 0 10)	0.12	0.114	0.12